



Computational identification of the safety regime of Li-ion battery thermal runaway

Liwen Zhang, Peng Zhao*, Meng Xu, Xia Wang

Department of Mechanical Engineering, Oakland University, Rochester, MI 48309, USA

HIGHLIGHTS

- Concepts of critical states and safety regime are demonstrated for Li-ion battery.
- Key kinetic features and dominant parameters of thermal runaway are identified.
- Effects of electrode material properties on thermal runaway are evaluated.
- Heat release distribution and evolution is shown for typical internal short circuit.
- A combined model of thermal-electrochemical and thermal runaway is demonstrated.

ARTICLE INFO

Keywords:

Thermal runaway
Critical runaway state
Safety regime
Internal short circuit (ISC)
Multiphysics modeling

ABSTRACT

Internal short circuit (ISC) and the subsequent electrochemical heat release is frequently a direct cause to trigger Li-ion battery thermal runaway. In this work, a decouple-recombine modeling approach is adopted to reveal the feature of thermal runaway induced by a typical ISC event. The thermal response and chemical kinetic feature of thermal runaway is computationally investigated in a three-dimensional configuration with assigned heat source intensity and duration. The threshold runaway state and the safety regime diagram are identified, corresponding to a pair of critical heat source intensity and critical duration time. Consequently, a safety regime diagram is computationally identified to distinguish the thermal runaway zone and safety zone. Simulation and analysis has been conducted to evaluate the dominant physical-chemical parameters, and the dependence of cathode material during thermal runaway. Meanwhile, the power dissipation during a representative ISC scenario is analyzed, where the local current could be an order of magnitude higher than that for a regular 1C discharge, and the maximum heat release rate is around 10^{12} W/m³. This heat release is input as source in the thermal runaway simulation, to demonstrate the coupling of the ISC and thermal abuse models. This work provides useful guidance to the fundamental understanding and prediction of thermal runaway phenomena induced by internal short circuit in Li-ion batteries.

1. Introduction

According to a recent projection made by the US Energy Information Administration (EIA), the combined share of sales attributable to gasoline and flex-fuel vehicles declines from 93% in 2018 to 75% in 2050 due to the growth in battery electric vehicle (BEV), plug-in hybrid electric vehicle (PHEV), and hybrid electric vehicle (HEV) scales [1]. As an advanced power storage medium, the development of Li-ion battery has attracted extensive research interest, as reviewed in [2–4].

Most previous research efforts target three major fundamental challenges of Li-ion battery, i.e., low energy density, undesired irreversible change and strong dependence on temperature. Specifically,

the first fundamental challenge in Li-ion battery development and implementation is its relatively low energy density compared to conventional energy sources, such as petroleum based fuels. The specific energy of gasoline is approximately 45 MJ/Kg, while the value for the state of art Li-ion battery is around 250 Wh/Kg [4], leading to a specific energy density ratio of 50 between gasoline and battery. This partly leads to the large size of battery packs in vehicles and slow charging issue, and has become a primary driving force for the development of new battery materials and chemistry. The second challenge is induced by the irreversible physical-chemical change such as degradation and aging [5]. The formed internal fracture or other unwanted physical structure change, e.g., Lithium-dendrite, during multiple charge-

* Corresponding author.

E-mail address: pengzhao@oakland.edu (P. Zhao).

<https://doi.org/10.1016/j.apenergy.2019.114440>

Received 3 October 2019; Received in revised form 29 November 2019; Accepted 21 December 2019

Available online 30 December 2019

0306-2619/ © 2019 Elsevier Ltd. All rights reserved.

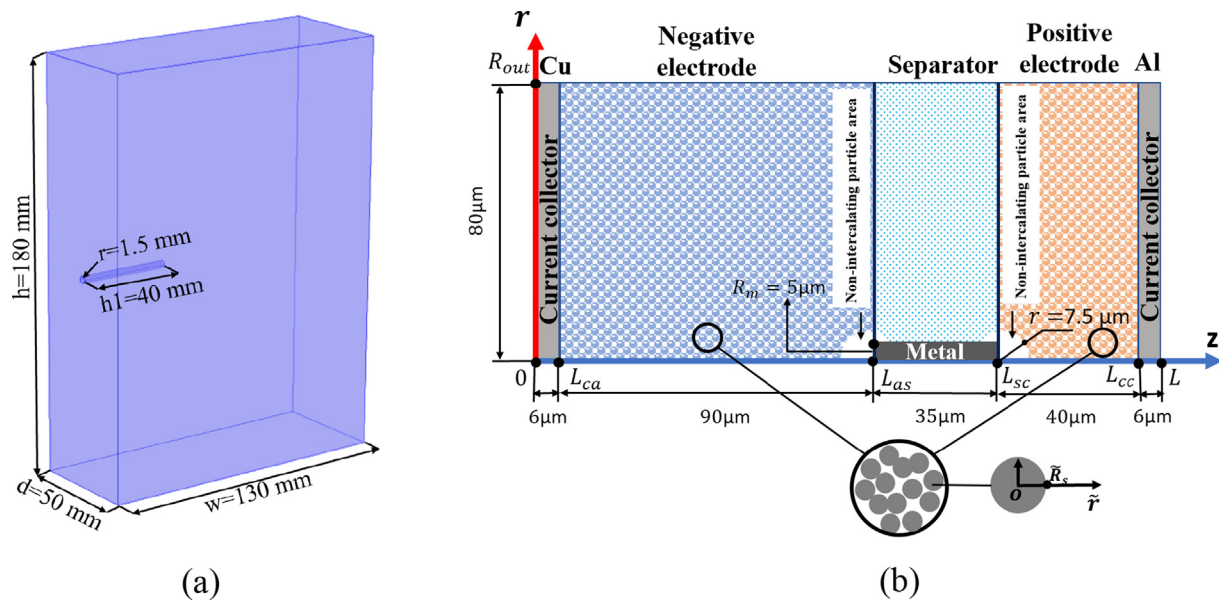


Fig. 1. (a) A 3D configuration of a prismatic cell for the simulation of thermal runaway, including a cylindrical region representing nail penetration; (b) A 2D unit cell model with metal penetrating the separator for internal short circuit modeling.

discharge cycling adds to more resistance for Li ion transfer and aggravates cycle-to-cycle and cell-to-cell variations [6] and may even cause failure and thermal runaway [7]. The third primary challenge is induced by the temperature sensitivities of Li-ion batteries. At relatively low temperatures, Li-ion batteries suffer from slow ion and charge transfer rate as well as slow electrochemistry, exhibiting high internal resistance and meanwhile aggravating the formation and growth of Li dendrite [7]. This feature intrinsically limits the cold performance of Li-ion batteries, however, it could be still improved by designing various heating protocols [8]. Under high temperature abuse or accidental conditions [9–15], undesired reactions such as Solid-Electrolyte-Interphase (SEI) decomposition, reaction between electrodes and electrolyte, and electrolyte decomposition, etc., can occur inside of the battery, leading to thermal runaway and subsequent explosion hazard [16–19]. In addition to these major challenges, the development of low-cobalt cathode material and battery recycling technology has attracted extensive interest, due to the environmental concerns from battery manufacturing and disposal.

Among these fundamental challenges and opportunities, the most urgent one is the monitor and prediction of thermal runaway, since it directly threatens properties and human lives. The mechanisms of thermal runaway are classified into mechanical abuse, electrical abuse and thermal abuse, and have been systematically reviewed in [20]. According to the survey conducted in [20], almost all reported EV accidents are associated with fire caused by thermal runaway, mostly likely, triggered by short circuit. The first and mostly adopted thermal runaway model of Li-ion batteries was developed by Hatchard et al. [16], where kinetic parameters of chemical reactions between electrodes and electrolyte were measured and calibrated from accelerating rate calorimetry (ARC) and differential scanning calorimeter (DSC), and the model results fit well with the oven exposure test for 18,650 LiCoO₂/graphite cell. Later, Spotnitz et al. [17] did a more systematic review of thermal behavior of components in Lithium-ion battery and a more complete set of exothermic reactions including the reaction of electrolyte decomposition. Based on these understanding, Kim et al. [18] developed a thermal abuse model and applied it to a 3D lithium ion battery configuration, further accounting for cell geometry and anisotropy of material thermal properties and successfully demonstrated the multidimensional behaviors of Li-ion battery thermal runaway. Since then, this thermal abuse model and simulation approach has been adopted in various studies related to Li-ion battery thermal

runaway [21–29]. These studies, for instance, include the influence of different material properties [21], the effectiveness of cooling system on runaway and propagation prevention [22] as well as thermal runaway under different experimental conditions such as constant-power heating test [23], overcharge [24], nail penetration [25] and internal short circuit [26]. Submodels including battery aging and other factors have also been developed [30] and combined with this thermal abuse model.

Although Li-ion battery thermal runaway is largely cell and material dependent, there are intrinsic common features rooted in this class of phenomena, in that it is always thermally initiated by a hot spot, followed by undesired exothermic chemical reactions triggered at elevated temperatures. Therefore, Li-ion battery thermal runaway is intrinsically an ignition problem. With the widely adopted and validated models for thermal runaway and the electrochemistry, the goal of the current work is to answer three of the most critical questions regarding thermal runaway and ISC of Li-ion batteries: (1) What is the threshold condition, i.e., power density (in W/m³) and duration, for a hot spot to trigger Li-ion thermal runaway? (2) What are the chemical kinetic features and key parameters during thermal runaway? (3) For a typical ISC scenario, how large is the heat release rate, and will it be sufficient to trigger thermal runaway?

2. Configuration and modeling methodology

2.1. Configuration

As shown in Fig. 1(a), a 3D box configuration with a cylinder region is adopted to represent a prismatic battery with nail penetration for the thermal runaway modeling part. The dimensions of the domain are 180 mm (height) × 130 mm (width) × 50 mm (depth) [22]. A cylindrical region of 1.5 mm (radius) × 40 mm (length) is placed perpendicular to the left surface. In this configuration, thermal runaway is triggered by two dominant physical-chemical processes: heat transfer from the cylindrical region with an artificially assigned uniform heat source intensity Q (W/m³) and duration time dt (s), and the runaway chemical kinetics involving the electrodes and electrolyte that contribute to heat generation within the bulk of battery.

The energy conservation equation of the computational domain is shown in the following:

$$\frac{\partial(\rho c_p T)}{\partial t} = \nabla \cdot (k \nabla T) + S \quad (1)$$

where ρ is the density, c_p is the heat capacity, k is the thermal conductivity, T is temperature. In the main computational domain within the cell, $S = S_{sei} + S_{ne} + S_{pe} + S_e$, the meaning of these heat source terms related to thermal runaway is explained in Section 2.2. Given the much larger size of the battery compared to a single layer of cathode-separator-anode, the thermal runaway reactions are assumed to be uniformly distributed within the cell. While in the cylindrical region, we have $S = \begin{cases} Q & (t < dt) \\ 0 & (t \geq dt) \end{cases}$, representing a uniform heat source lasting a certain duration time. Due to the multi-layered structure of the Li-ion battery, the anisotropic thermal conductivity of the battery (through-plane and in-plane) is considered. The values of thermal properties of a typical LiCoO₂/graphite battery are listed in Table 1 of the Supplementary Material.

To understand the actual heat generation rate (in W/m³) from a typical internal short circuit (ISC) event, a 2D unit cell model is developed for thermal-electrochemical modeling, including copper negative current collector, a porous negative electrode (typically made of graphite), an ion-conductive but electron-insulating separator, a porous positive electrode made of Li and transition metal oxide, aluminum positive current collector and a piece of Aluminum metal directly connecting two electrodes. The structure and thickness of each layer is shown in Fig. 1(b). A liquid electrolyte permeates the electrodes and separator region. The solid-phase in electrodes is described by a lattice of spherical particles with uniform size, representing the intercalation center for metallic Li diffusion. During a typical discharging process, metallic Li is deintercalated out of the anode. An equal amount of Li ion and electrons are generated at the electrode-electrolyte interface of each spherical particle. These Li ions are transferred through the electrolyte, across the separator, to the cathode; while the electrons migrate through the external circuit and back to the positive current collector, and eventually recombine with these Li ions. Consequently, these metallic Li atoms eventually intercalate into each solid spherical particles. By design, electrons are not allowed to penetrate the separator and are forced to go through the external circuit under this normal discharging condition. For simplicity, ISC in the current work is triggered by a piece of Aluminum that directly connects the positive and negative electrodes, which creates an alternative path for the migration of electrons within the battery.

The mass and charge conservation equations, energy conservation and the electrochemical kinetics given by Butler-Volmer equation are solved together following the configuration in Fig. 1(b), subject to properly given boundary conditions. More details on ISC thermal electrochemical modeling are provided in Section 2.3. The power dissipation density (in W/m³) is then calculated to measure rate of energy dissipation and heat release from the electrochemical system to the thermal system.

2.2. Thermal runaway modeling

The thermal runaway models demonstrated in [16–19] are briefly reviewed and adopted in the current study. Solid electrolyte interface (SEI) formed during the first cycle in Li-ion batteries plays a vital role in preventing the side reaction between the electrodes and electrolyte. This layer is metastable and can decompose exothermically at elevated temperature. The corresponding reaction can be expressed in the following equations:

$$S_{sei}(T, c_{sei}) = -H_{sei} W_c \frac{dc_{sei}}{dt} \quad (2)$$

$$\frac{dc_{sei}}{dt} = -A_{sei} \exp\left(-\frac{E_{a,sei}}{RT}\right) c_{sei}^{m_{sei}} \quad (3)$$

where $S_{sei}(T, c_{sei})$ is the heat release rate from the SEI decomposition,

which depends on the dimensionless amount of lithium-containing meta-stable species (c_{sei}) in the SEI, the temperature of the battery (T) and the battery material.

Once the SEI layer starts to decompose, it cannot protect the negative electrode from contacting with the electrolyte such that the exothermic reaction between the intercalated lithium and electrolyte can occur:

$$S_{ne}(T, c_{ne}, t_{sei}) = -H_{ne} W_c \frac{dc_{ne}}{dt} \quad (4)$$

$$\frac{dc_{ne}}{dt} = -A_{ne} \exp\left(-\frac{t_{sei}}{t_{sei,ref}}\right) c_{ne}^{m_{ne,n}} \exp\left(-\frac{E_{a,ne}}{RT}\right) \quad (5)$$

$$\frac{dt_{sei}}{dt} = A_{ne} \exp\left(-\frac{t_{sei}}{t_{sei,ref}}\right) c_{neg}^{m_{ne,n}} \exp\left(-\frac{E_{a,ne}}{RT}\right) \quad (6)$$

where $S_{ne}(T, c_{ne}, t_{sei})$ is the heat release rate from the negative-electrolyte reaction. It depends on the dimensionless amount of lithium intercalated within the carbon (c_{ne}), the dimensionless measure of SEI layer thickness (t_{sei}), the temperature of the battery (T) and other material properties.

At oxidized state, the positive material reacts directly with the electrolyte. The chemical reduction of the positive active material with the electrolyte is highly exothermic:

$$S_{pe}(T, \alpha) = H_{pe} W_p \frac{d\alpha}{dt} \quad (7)$$

$$\frac{d\alpha}{dt} = A_{pe} \alpha^{m_{pe,p1}} (1 - \alpha)^{m_{pe,p2}} \exp\left(-\frac{E_{a,pe}}{RT}\right) \quad (8)$$

where $S_{pe}(T, \alpha)$ is the heat release rate from the positive electrode-electrolyte reaction. It depends on the degree of conversion (α), the temperature of the battery (T) and the material properties of the battery.

Eventually, the electrolyte can also decompose exothermically at elevated temperatures:

$$S_e(T, c_e) = -H_e W_e \frac{dc_e}{dt} \quad (9)$$

$$\frac{dc_e}{dt} = -A_e c_e^{m_e} \exp\left(-\frac{E_{a,e}}{RT}\right) \quad (10)$$

where $S_e(T, c_e)$ is the heat release rate from the electrolyte decomposition, depending on the dimensionless concentration of electrolyte (c_e), the temperature of the battery (T), and the materials properties of the battery.

Depending on the battery materials, parameters involved in this thermal runaway model could be calibrated using ARC, DSC and TGA analysis, such that the model exhibits satisfactory predictability for thermal runaway behavior. A detailed nomenclature including parameter values for a typical LiCoO₂/graphite battery is listed in Table 2 of the Supplementary Material. It is also worth noting that since we are interested in very fast runaway process (with delay time around 10 s), during which the cooling design on the surface of a battery can hardly be effective, the thermal boundary conditions are hence intentionally set as adiabatic. Such simplification can also help to rule out the uncertainty of threshold ignition energy induced by the ambiguity in boundary conditions, as shown in the following sections.

2.3. A 2D Thermal-electrochemical model of internal short circuit

The thermal-electrochemical model adopted in the current ISC simulation is based on previous studies [31–43]. Five conservation equations are solved together, linked by the constitution relation of the electrochemistry Butler-Volmer equation. These equations include: (1) Metallic Li mass conservation in the solid phase; (2) Li ion mass

conservation in the liquid phase; (3) the electron charge conservation in the solid phase; (5) the Li ion charge conservation in the liquid phase; (5) Energy conservation equation describing temperature evolution. Based on the current 2D cylindrical configuration for ISC with metal penetration as in Fig. 1(b), a detailed introduction to the thermal-electrochemical model and its boundary conditions is given below.

2.3.1. Mass conservation of lithium in the solid phase

The solid phase in the electrodes is modeled as a lattice of spherical particles with uniform size. Within each particle, the intercalation and deintercalation of Li atom follows Fick's law of diffusion in polar coordinates:

$$\frac{\partial c_s}{\partial t} = \frac{D_s}{r^2} \frac{\partial}{\partial r} \left(r^2 \frac{\partial c_s}{\partial r} \right) \quad (11)$$

where c_s is the concentration of lithium in the active material particles of electrode, r is the radial coordinate, D_s is the solid phase diffusivity of Li atom.

At the center of the particle, zero flux is specified from symmetry, while the species flux in and out the particle surface is related to the local current density:

$$\frac{\partial c_s}{\partial r} \Big|_{r=0} = 0 \quad (12)$$

$$-D_s \frac{\partial c_s}{\partial r} \Big|_{r=R_s} = \frac{i_{loc}}{F} \quad (13)$$

2.3.2. Mass conservation of lithium ions in the electrolyte phase

The transport of lithium ions in the electrolyte phase follows Fick's diffusion law and the electromigration:

$$\frac{\partial c_l}{\partial t} = \nabla \cdot (D_{l,eff} \nabla c_l) + a_s \frac{(1 - t_+)}{F} i_{loc} \quad (14)$$

where c_l is the lithium ion concentration in the electrolyte, ε_l is the volume fraction of the electrolyte phase, a_s is the specific interfacial area, i_{loc} is the electrode current density, t_+ is the transference number of lithium ions, $D_{l,eff}$ is the effective diffusion coefficient given by the Bruggeman relation:

$$D_{l,eff} = D_l \varepsilon_l^{1.5} \quad (15)$$

Zero flux boundary conditions are set at the interface with current collectors, metal surface and the outer radial surface due to no ion penetration [35,37]. Zero flux boundary conditions are also given along the axis with $r = 0$ from symmetry. These boundary conditions are listed below:

$$\frac{\partial c_l}{\partial r} \Big|_{r=0} = 0 \quad (16)$$

$$\frac{\partial c_l}{\partial r} \Big|_{r=R_{out}} = 0 \quad (L_{ca} < z < L_{cc}) \quad (17)$$

$$\frac{\partial c_l}{\partial z} \Big|_{z=L_{as}} = \frac{\partial c_l}{\partial z} \Big|_{z=L_{sc}} = 0 \quad (0 < r < R_m) \quad (18)$$

$$\frac{\partial c_l}{\partial z} \Big|_{z=L_{ca}} = \frac{\partial c_l}{\partial z} \Big|_{z=L_{cc}} = 0 \quad (19)$$

$$\frac{\partial c_l}{\partial r} \Big|_{r=R_m} = 0 \quad (L_{as} < z < L_{sc}) \quad (20)$$

2.3.3. Charge conservation in the solid phase of electrodes

Charge in the solid phase is contributed by electrons. The governing equation for the electrical charge balance in the electrodes is described by:

$$\nabla \cdot i_s = -a_s i_{loc} \quad (21)$$

where a_s is the specific interfacial area which characterizes electrode

performance:

$a_s = \frac{3\varepsilon_s}{R_s} (22) i_s$ is the electrical current density in the solid phase as described by ohm's law:

$i_s = -\sigma_{s,eff} \nabla \phi_s (23)$ where ϕ_s is the solid phase potential, $\sigma_{s,eff}$ is the effective solid-phase electrical conductivity, depending on the electrical conductivity of the bulk material and the porosity, following the Bruggeman relation:

$$\sigma_{s,eff} = \sigma_s \varepsilon_s^{1.5} (24)$$

At the solid-electrolyte interface (SEI) (excluding interface with the metal), zero electrical current boundary condition is specified:

$$\frac{\partial \phi_s}{\partial z} \Big|_{z=L_{as}} = \frac{\partial \phi_s}{\partial z} \Big|_{z=L_{sc}} = 0 \quad (R_m < r < R_{out}) \quad (25)$$

Symmetry boundary is applied for solid-phase potential along the axis of $r = 0$, and insulation boundary condition is applied on the outer radial surface of solid-phase in the electrodes:

$$\frac{\partial \phi_s}{\partial r} \Big|_{r=0} = 0 \quad (26)$$

$$\frac{\partial \phi_s}{\partial r} \Big|_{r=R_{out}} = 0 \quad (L_{ca} < z < L_{cc}) \quad (27)$$

2.3.4. Charge conservation in the electrolyte

Current in the electrolyte is contributed by the migration and diffusion of Li ions. Transport of lithium ions in the electrolyte can be described by the balance equation for ionic current density i_l :

$$\nabla \cdot i_l = a_s i_{loc} \quad (28)$$

$$i_l = -\nabla \phi_l + \left(\frac{2\sigma_{l,eff} RT}{F} \right) (1 + \frac{\partial \ln f_{\pm}}{\partial \ln c_l}) (1 - t_+) \nabla \ln c_l \quad (29)$$

where ϕ_l is the potential in the liquid phase, f_{\pm} is the average molar activity coefficient, $\sigma_{l,eff}$ is the effective ionic conductivity in the electrolyte:

$$\sigma_{l,eff} = \sigma_l \varepsilon_l^{1.5} \quad (30)$$

Along the axis $r = 0$, symmetric boundary condition is again assigned for ϕ_l . At the interface of current collector and electrode and the outer axial surface of the electrodes and separator, zero flux boundary condition for ionic current is specified due to non-ion penetration:

$$\frac{\partial \phi_l}{\partial r} \Big|_{r=0} = 0 \quad (31)$$

$$\frac{\partial \phi_l}{\partial z} \Big|_{z=L_{ca}} = \frac{\partial \phi_l}{\partial z} \Big|_{z=L_{cc}} = 0 \quad (32)$$

$$\frac{\partial \phi_l}{\partial r} \Big|_{r=R_{out}} = 0 \quad (L_{ca} < z < L_{cc}) \quad (33)$$

2.3.5. Electrochemical kinetics

To bring a closure to this model, a constitution relation that correlates the current density with overpotential is needed. The electrode current density is given by Butler-Volmer equation:

$$i_{loc} = i_0 \left[\exp \left(\frac{\alpha_a F \eta}{RT} \right) - \exp \left(\frac{-\alpha_c F \eta}{RT} \right) \right] \quad (34)$$

where i_0 is the exchange current density, α_c denotes the cathodic charge transfer coefficient and α_a denotes the anodic charge transfer coefficient. These two coefficients are equal to each other [44]. η is the activation over potential, F is the Faraday constant, R is the universal gas constant.

The exchange current density is calculated by:

$$i_0 = F k_0 (c_l)^{\alpha_a} (c_{s,max} - c_s)^{\alpha_a} (c_s)^{\alpha_c} \quad (35)$$

where k_0 is a rate constant, $c_{s,max}$ is the maximum solid-phase Li

concentration, the activation over potential η is defined as the potential difference between the operating voltage and the thermodynamic equilibrium potential U_{eq} :

$$\eta = \phi_s - \phi_l - U_{eq} \quad (36)$$

where the equilibrium potential U_{eq} is a function of both the state of charge and temperature:

$$U_{eq} = U_{eq,i} + \frac{\partial U_{eq,i}}{\partial T}(T - T_{ref}) \quad (37)$$

The state of charge could be determined by the relative portion of Li in the electrodes. For example, in a LCO battery with positive electrode Li_xCoO_2 and negative electrode Li_yC_6 , $U_{eq,i}$ and $\frac{\partial U_{eq,i}}{\partial T}$ for both electrodes can be provided as functions of Li stoichiometric ratios x or y , as discussed in [45,46].

2.3.6. Energy conservation

In general, ignoring the internal contact resistance, internal heat generation of a Li ion battery comes from three sources: (1) heat generation due to entropy changes in the material structure during charging and discharging, which is frequently referred to as the reversible entropic heat $q_{rev} = a_s i_{loc} T \frac{\partial U_{eq}}{\partial T}$, (2) heat generation from irreversible electrochemical reactions, as manifested by the reaction current and overpotential $q_{irr} = a_s i_{loc} \eta$; (3) heat generation from electron conduction in the solid phase, and the migration and diffusion of Li ion in the electrolyte, which is referred to as ohmic heat q_{ohm} . Here, accounting for the heat generation from reversible entropic heat q_{rev} , irreversible reaction heat q_{irr} and ohmic heat q_{ohm} , the energy conservation is:

$$\rho C_p \frac{\partial T}{\partial t} = \lambda \nabla^2 T + q_{rev} + q_{irr} + q_{ohm} \quad (38)$$

The ohmic heat consists of three terms: electrical ohmic heat $q_{ohm,s}$, ionic ohmic heat $q_{ohm,l}$ and internal short circuit heat $q_{ohm,m}$ in the metal or current collector, that gives:

$$\begin{aligned} q_{ohm} &= q_{ohm,s} + q_{ohm,l} + q_{ohm,m} \\ &= -i_s \cdot \nabla \phi_s - i_l \cdot \nabla \phi_l - i_m \cdot \nabla \phi_m \end{aligned} \quad (39)$$

Adiabatic boundary conditions are applied to all the boundaries in Fig. 1(b).

2.3.7. Governing equations in metal, current collector and non-intercalating particle area

The governing equation for the electrical charge balance in the metal or current collector is described by:

$$\nabla \cdot i_m = 0 \quad (40)$$

where i_m is the electrical current density in the solid metal phase. The electron transfer in the solid metal phase is described by ohm's law:

$i_m = -\sigma_m \nabla \phi_m$ (41) where σ_m is the metal electrical conductivity, and ϕ_m is the potential in the metal.

At the interfaces of current collector-electrode, metal-electrode and metal-separator, due to the electron-conduction and ion-insulation feature, zero flux of ionic current conditions are satisfied to ensure the consistency in the electronic charge flux. It is worth noting that a quarter-circle non-intercalating particle region is assigned at each end of the metal to ensure the consistency of non-ion penetration condition approaching the metal surface. Compared to regular solid-phase, the only difference in this non-intercalating particle region is that while the solid phase is still electron conductive, Li ions are not allowed to enter this region. Therefore, this non-intercalating region is considered similar to metal or current collector as an electron conductor, such that the only governing equation is electron charge conservation.

The boundary conditions at the current collectors are related to the flux of charge in and out of the electrode. At the current collector, insulation is specified for electrical current in solid phase [31,33,37]:

$$\frac{\partial \phi_s}{\partial z} \Big|_{z=0} = \frac{\partial \phi_s}{\partial z} \Big|_{z=L} = 0 \quad (42)$$

The negative electrode terminal is grounded, the positive electrode terminal is the cell voltage corresponding to SOC = 100% and the rest of the outer axial boundaries are set to be electrically insulated:

$$\phi_s \Big|_{r=R_{out}} = 0V \quad (0 < z < L_{ca}) \quad (43)$$

$$\phi_s \Big|_{r=R_{out}} = 4.3V \quad (L_{cc} < z < L) \quad (44)$$

2.4. Numerical methods

Both thermal runaway and ISC cases are solved by commercial software COMSOL Multiphysics 5.3. In the thermal runaway simulation, a domain ODE model is used to account for the heat generation due to the chemical reactions. The fastness of the chemical reactions could place substantial difficulty on the usage of explicit CFD solvers and requires tiny integration time step, which is frequently referred as the chemical stiffness [47]. Therefore, we choose the backward differentiation formula (BDF) method to set as the time stepping method, one of the available implicit time-dependent solvers, with the maximum BDF order of 5 and minimum BDF order of 2. The relative tolerance and absolute error tolerance are set as 1E-6 and 1E-8 respectively. In the ISC simulation, we choose time-dependent solver using BDF for time marching, with the maximum BDF order of 2 and minimum BDF order of 1.

Grid independence study has been conducted for both scenarios by using three different mesh specifications, varying from sparse to dense. As shown in Fig. S1 and S2 in the Supplementary Material, the maximum temperature evolution during thermal runaway, and the average power dissipation during ISC event using meshes with different levels of refinement exhibits negligible difference, we have hence demonstrated the meshes adopted are sufficient for simulation.

2.5. Model validation

Both the thermal runaway and thermal-electrochemical models are extensively validated against literature reported experimental data, and all the comparisons are further supplied as Figs. 3–7 in the Supplementary Material. Specifically, the thermal runaway model is validated against experimental targets acquired in oven exposure tests under iso-thermal [22], constant heating rate [13], and near adiabatic conditions [13]. The thermal-electrochemical model is validated against experimental data including surface temperature under constant discharging rate [48], temperature and battery voltage measurement at different discharging rates [45,49]. These data also cover all different battery materials and chemistry involved in the current work, and all comparisons show very good quantitative agreement as such provide great confidence in the simulation results.

It is also noted that although more detailed thermal runaway models have been developed recently based on thermal calorimetry measurement [13], the model we adopted is so far the most widely-used one and is being applied in battery research until very recently [19]. To make sure the conclusion is not affected by the difference in the thermal runaway models, we have used our model and parameters to simulate the same two sets of oven tests in [13] and compared with their simulation. As shown in Figs. S4-a&b, the current model has quantitative agreement with the detailed simulation and the oven test data. This adds to great confidence to the current model for the prediction of thermal runaway onset condition, and confirms that the concepts and conclusions will not change with changes in cell chemistry.

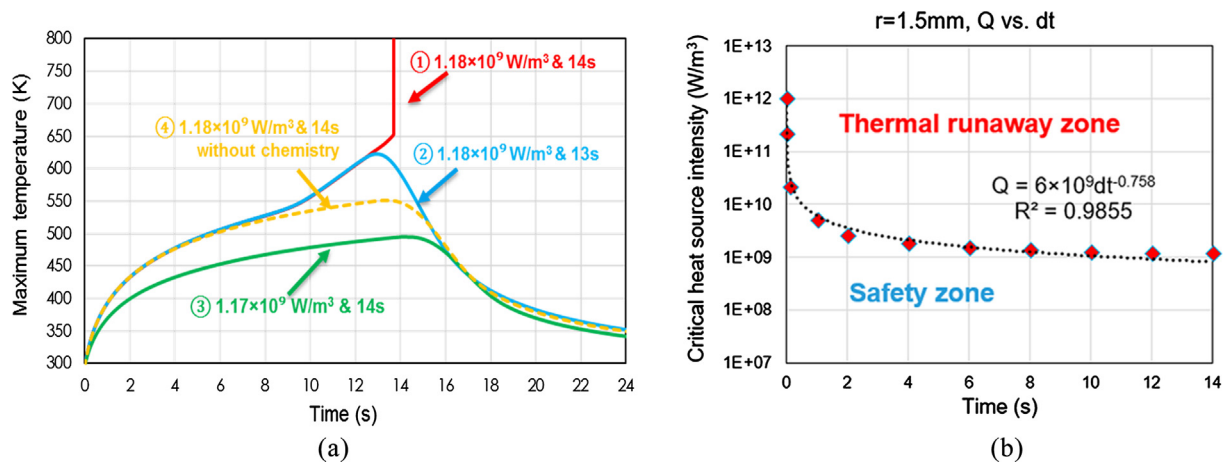


Fig. 2. (a) Comparison of maximum temperature history of runaway and non-runaway cases, demonstrating the concept of critical runaway state. (b) Safety regime of a LiCoO₂/Graphite battery shown by critical heat source intensity and duration, with heat source radius 1.5 mm.

3. Results and discussion

3.1. Critical state and safety regime of thermal runaway

Thermal runaway of Li-ion battery has become a major concern of societal safety. Fundamentally, it is also a problem featured by reaction-transport coupling, similar to the combustion process. One of the key combustion concepts is the minimum ignition energy [50], which characterizes the critical amount of energy needed to successfully trigger a flame in a reactive mixture by an ignition kernel. Made of explosive materials, Li-ion batteries tend to ignite and explode when an internal heat source is beyond a certain threshold. Hence, to understand and predict the safety regime of a Li-ion battery, we ask the same question on Li-ion batteries based on the concept of minimum ignition energy: What is the critical power needed to trigger thermal runaway by a hot spot?

To capture the critical condition that can trigger thermal runaway in the delay time of interest, different combinations for heat source intensity (Q) and duration time (dt) in the cylindrical region have been applied in the configuration shown in Fig. 1(a). Fig. 2(a) compares the maximum temperatures for four different heat source intensities and durations, to demonstrate the phenomena of thermal runaway. For the base Case 1 with $Q = 1.18\text{E}9 \text{ W/m}^3$ and duration time $dt = 14 \text{ s}$, the maximum temperature gradually increases in the initial period and then sharply rises and achieves ignition right before 14 s. The substantial heat release rate and fast temperature rise indicates thermal runaway. Starting from this benchmark Case 1, by reducing either the duration time of heat source to $dt = 13 \text{ s}$ (Case 2) or the heat source intensity to $Q = 1.17\text{E}9 \text{ W/m}^3$ (Case 3), the maximum temperature reaches a local maximum and decays due to heat conduction. Consequently, no thermal runaway phenomenon has been observed for these two cases. The sensitive dependence of runaway event on the heat source intensity and duration time has allowed us to identify the critical runaway state. Such critical state corresponds to a pair of critical heat source intensity and duration time, below which thermal runaway cannot occur.

Typically, a combined thermal-chemical mechanism is adopted to explain phenomena of ignition and explosion nature [51], where positive feedback exists between the temperature rise and the rate of major exothermic reactions in a system. The next question is then: what are the thermal and chemical effects from the runaway reactions during a typical runaway event? We have therefore conducted simulation with another Case 4, with the same heat source intensity and duration time as Case 1, yet without the thermal runaway chemical source terms. Clearly, deviation between Case 1 and Case 4 does not appear until about 6 s, indicating the negligible role of heat release from thermal

runaway chemistry during this period. By combining the information shown later in Fig. 4, the negligible thermal effect from SEI decomposition in this period is hence identified. After that, the maximum temperature of Case 1 starts to build up, as induced by runaway exothermic reactions.

By calculating the critical runaway states with different combinations of threshold heat source intensity and duration time, we have successfully identified a safety regime diagram for Li-ion batteries, as shown in Fig. 2(b). Below this curve, a hot spot either does not contain sufficient power or does not last for sufficient residence time, thermal runaway cannot be triggered; while above the curve, ignition occurs due to elevated hot spot intensity and/or extended duration. This curve is fitted to a power law form as $Q = 6\text{E}9 dt^{-0.758}$ (Q in W/m^3 and dt in s). With shorter duration, the critical Q is more sensitive to dt ; while for longer duration time, such dependence becomes less and less sensitive. This formula can provide useful guidance for battery safety prediction and control. As shall be discussed later, this safety regime depends on battery materials, the hot spot size and potentially cooling conditions for sufficiently long ignition delays. The concept of critical runaway state and the computational methodology we have developed is however general, and could be extended to arbitrary Li-ion batteries.

To further understand the geometric effect of the heat source, simulations have been conducted for different heat source radius with fixed heat source intensity ($Q = 1.18\text{E}9 \text{ W/m}^3$) and duration ($dt = 14 \text{ s}$) as Case 1 in Fig. 2(a). As seen in Fig. 3, compared to the base case with radius of 1.5 mm, the delay time of thermal runaway is substantially decreased to about 4 s, a 71.4% relative change, when the hot spot radius is increased to 2 mm by 33.3%. On the other hand, with a sufficiently small radius of the heat source, thermal runaway does not occur at all, as in the case of radius 1 mm in Fig. 3(a). The results are reasonable because the interface of the heat source plays a crucial role in heat transfer, and a larger radius indicates a larger surface area which can create a broader high temperature region for thermal runaway reactions to occur. With fixed $dt = 14 \text{ s}$, the critical heat source intensity needed to trigger thermal runaway is shown in Fig. 3(b). A monotonic decreasing trend is observed, where the threshold heat source intensity is less and less sensitive to hot spot size with increasing radius. A power law fitting formula has been obtained for the current LiCoO₂/graphite battery, showing $Q = 2\text{E}5 r^{-1.32}$.

3.2. Chemical kinetic feature and key parameters during thermal runaway

To gain insights into the chemical reaction most relevant to thermal runaway, we have compared the evolution of the dimensionless concentrations and other parameters for two cases with the same heat source $Q = 1.18\text{E}9 \text{ W/m}^3$, but different duration time dt . Consequently,

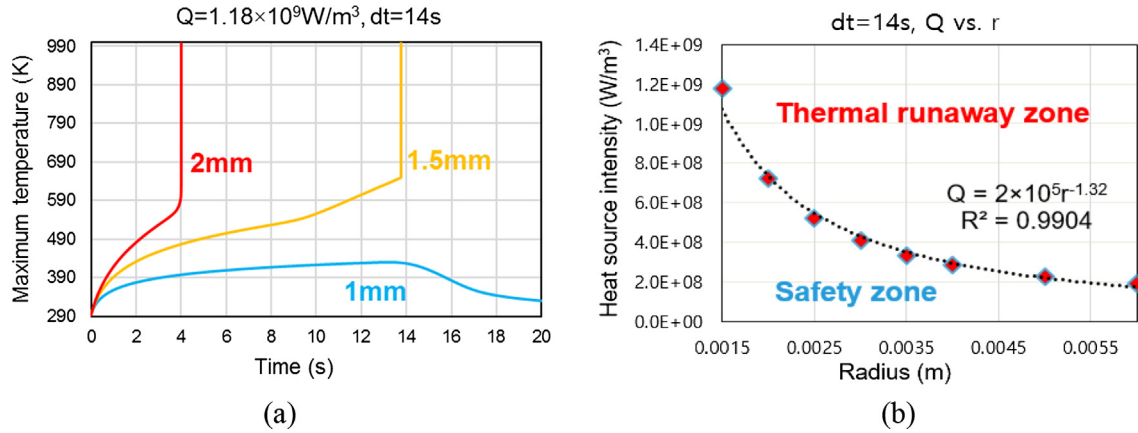


Fig. 3. (a) Evolution of maximum temperature for the heat source with same intensities and durations but different radius. (b) Safety regime of a $\text{LiCoO}_2/\text{Graphite}$ battery shown by critical heat source intensity and heat source radius, with fixed heat source duration 14 s.

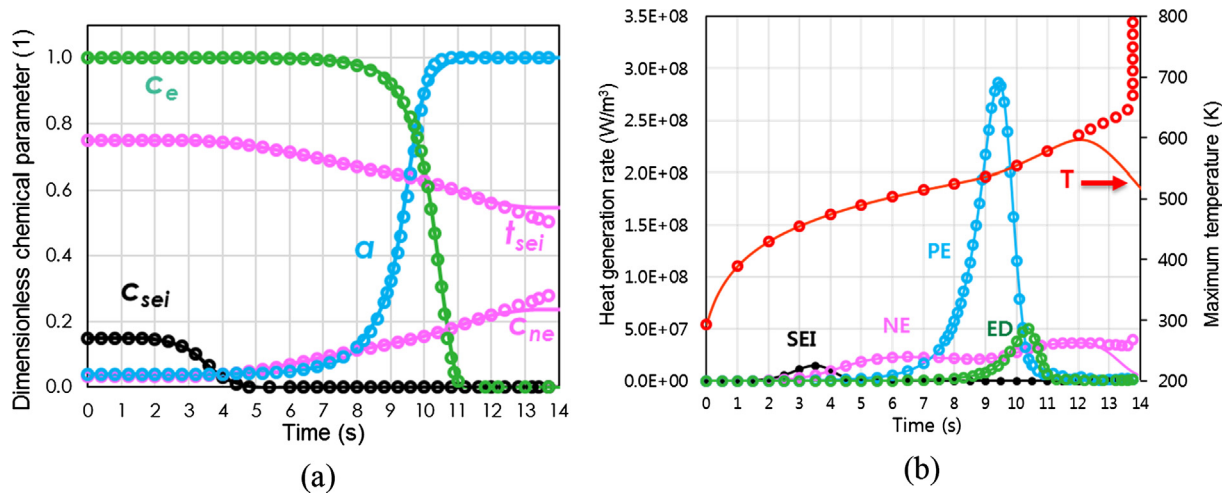


Fig. 4. Comparison of chemical kinetic feature of runaway (symbol) and non-runway (solid line) cases: (a) Evolution of the dimensionless concentrations in different thermal runaway reactions for a randomly selected point close to the interface (b) Evolution of heat generation rate from each chemical reaction.

the case with $dt = 14 \text{ s}$ is the same as Case 1 in Fig. 2(a), and thermal runaway is triggered; while the other case with $dt = 12 \text{ s}$ belongs to the safe regime below the threshold limit, and hence does not trigger thermal runaway. As shown in Fig. 4 (a), the only kinetic difference between the runaway and non-runway cases appears in the profiles of the dimensionless amount of lithium intercalated in the negative electrode (c_{ne}) and the dimensionless measure of SEI layer thickness (t_{se}), while the evolution of the rest dimensionless parameters overlaps. According to Eqs. (4)–(6), these differences will directly affect the heat release term S_{ne} , the reaction between the electrolyte and negative electrode, as shown in Fig. 4(b). Different from the other three reactions with a single peak, the heat release profile of negative electrode – electrolyte reaction has a broad, plateau-shape evolution profile and can last very long. The occurrence of thermal runaway is directly induced by the larger heat release from negative electrode-electrolyte reaction right before runaway occurs. It is also seen that the sequence of the four runaway reactions follow the order of SEI decomposition (SEI), negative electrode-electrolyte reaction (NE), positive electrode-electrolyte reaction (PE) and eventually electrolyte decomposition (ED). This order is also consistent with the understanding of battery stability and aging. It is generally considered that the SEI on the anode is more unstable due to the evident reduction reactions and the larger volume expansion of anode materials, compared to the SEI on the cathode [52,53].

To further identify the key thermal-chemical-physical parameter in affecting thermal runaway, we have conducted sensitivity analysis and

calculated the dimensionless sensitivity, as defined by: $\frac{\partial \ln \tau}{\partial \ln \chi}$, where τ is the ignition delay time for thermal runaway, defined as the duration from the starting point to the instant when the maximum temperature rise rate occurs, χ is any parameter of interest in the thermal runaway model, such as the reaction rate, density, and conductivity. This normalized sensitivity is defined in such a way that it does not have a dimension, and hence it helps to equally evaluate the significance of all the parameters involved in the model. When calculating the sensitivity, the same computation is repeated by only perturbing the parameter of interest by 5% while holding the values fixed for the other parameters. Consequently, this method is also referred to as the trial-and-error approach. For example, a normalized sensitivity of -3 means -15% of change in τ is expected if the target parameter is increased by 5%. The normalized sensitivity has been conducted for the frequency factors and activation energies in Eqs. (2), (4), (7), (9), cell density, heat capacity, heat conductivity in and through plane, as shown in Fig. 5 (a) and (b). For the chemical reactions, the rate of positive electrode-electrolyte reaction plays the most important role in affecting the delay time for thermal runaway. Regarding thermal physical parameters, the selected parameters exhibit similar value of normalized sensitivity and hence play similar roles in affecting the delay time. These calculations provide useful guidance on the usage and optimization of the thermal runaway model for validation purposes.

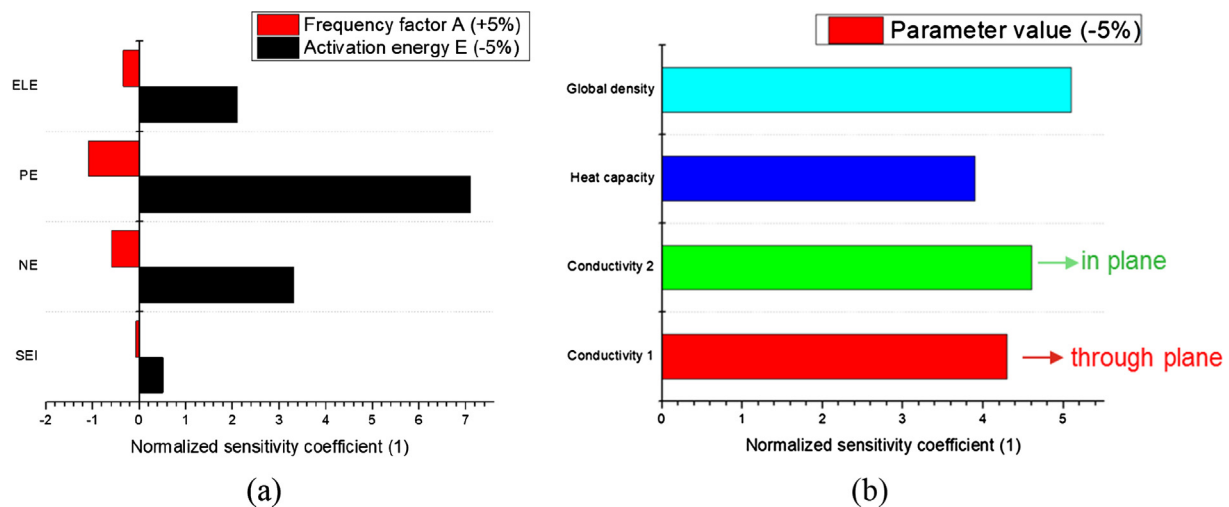


Fig. 5. Identification of key thermal runaway parameters using the model: (a) normalized sensitivity coefficients of chemical kinetic parameters including reaction rate constant and activation energy (b) normalized sensitivity coefficients of thermal physical parameters including density, specific heat capacity and conductivity.

3.3. Material effects of thermal runaway

Extensive research has been conducted looking for high density, stable, cheap and environment benign Li-ion battery materials. The thermal runaway model adopted in the current study has been validated against battery experiments of different electrode materials. Three batteries with unique thermal-chemical parameters are selected from the literature. As shown in Table 3 in the Supplementary Material, Battery 1 and 3 are both LiCoO₂/Graphite, while Battery 2 is NMC based. The runaway kinetic parameters of 1 and 3 are the same (as shown in the supplemental Table 2), however, their thermal conductivities are very different, according to measured data. As in Table 3, compared to Battery 1, thermal conductivity in and through plane is higher by 36.8% and 228.5% for Battery 3, respectively. This leads to a much broader safety region of Battery 3, as shown in Fig. 6. For the NMC Battery 2 (detailed runaway data provided in the supplemental Table 4), whose activation energy of anode-electrolyte is higher by 10.3%, a broader safety region is also observed from Fig. 6. Although conductivity in plane for Battery 2 is lower by 15.5% compared to LCO Battery 1, which is expected to narrow its safety regime, such an effect is however reversed by that from the elevated activation energy. The results have demonstrated the feasibility of predicting and comparing

the safety region of different Li ion batteries. Concerns on accurate measure of battery thermal properties are also raised, which can substantially affect the safety evaluation of different battery materials.

3.4. Heat release during an open-circuit internal short event

So far, the concepts of critical states and the regime of thermal runaway of different Li-ion batteries have been demonstrated, using artificially assigned heat source intensity and duration. In reality, an initial hot spot is most likely to be caused by heat release from electrochemical reactions in an ISC event. The question to be raised is therefore: how large is the heat release rate in a typical ISC scenario, and will it be sufficient to trigger thermal runaway? Based on the ISC configuration in Fig. 1(b) and the thermal-electrochemical model as described in Sec. 2, distribution and evolution of potential, current and temperature are calculated, based on which the heat release rate in a single-layer battery structure for three different batteries LCO, NMC and LFP can be evaluated. Parameters involved in the electrochemical models for these materials are taken from the literature [21,34,39,41–43,45,46,49,54–60] as detailed in Tables 5–7 in the Supplementary Material, and their performance validation is shown in Figs. 5–7.

As shown in Fig. 7(a), in the initial period of the electrical field development, the maximum heat release rate occurs in the metal region, due to the high potential drop and the high current. As the electrical field approaches equilibrium, the potential drop on the metal decreases for its low resistance, and the heat release rate in the metal region therefore starts to drop. In the meantime, heat release rate in the non-intercalating particles area on both sides of the metal gradually increases and becomes dominant, eventually forming a plateau. Depending on the material, the maximum heat release can appear on either side of the non-intercalating particle area. For example, maximum heat release rate occurs on the positive side of metal for LCO and LFP batteries, while it occurs on the negative side for NMC, as shown in the zoom-in subplot in Fig. 7(a). Regardless the battery material, relaxation time for the field to achieve equilibrium is around 1 ms, and the maximum local heat release rate in the whole field can be as high as 1E12 W/m³. The evolution of heat release shows both qualitative and quantitative agreement among the three battery materials, exhibiting negligible difference. This implies that the dominant effect in ISC heat release is largely electrical. The maximum temperature in these batteries can increase by 30 °C within 2 ms for this ISC event, equivalent to a temperature rise rate of 15000 °C/s. The LFP battery, however, exhibits the modest temperature increment, due to its slightly lower heat

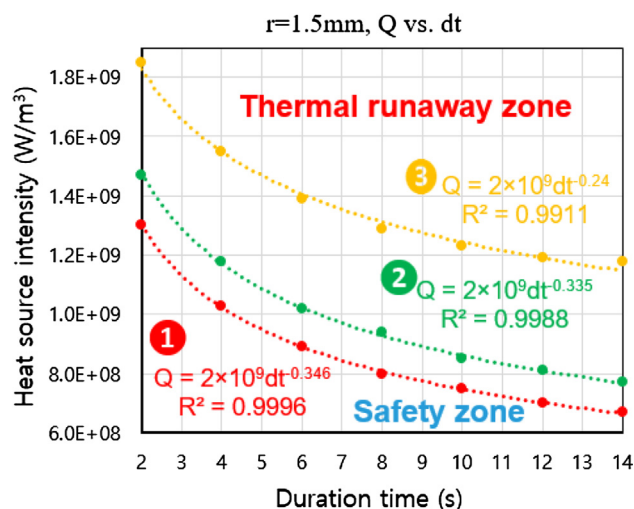


Fig. 6. Comparison of the thermal runaway regime of three different Li-ion batteries.

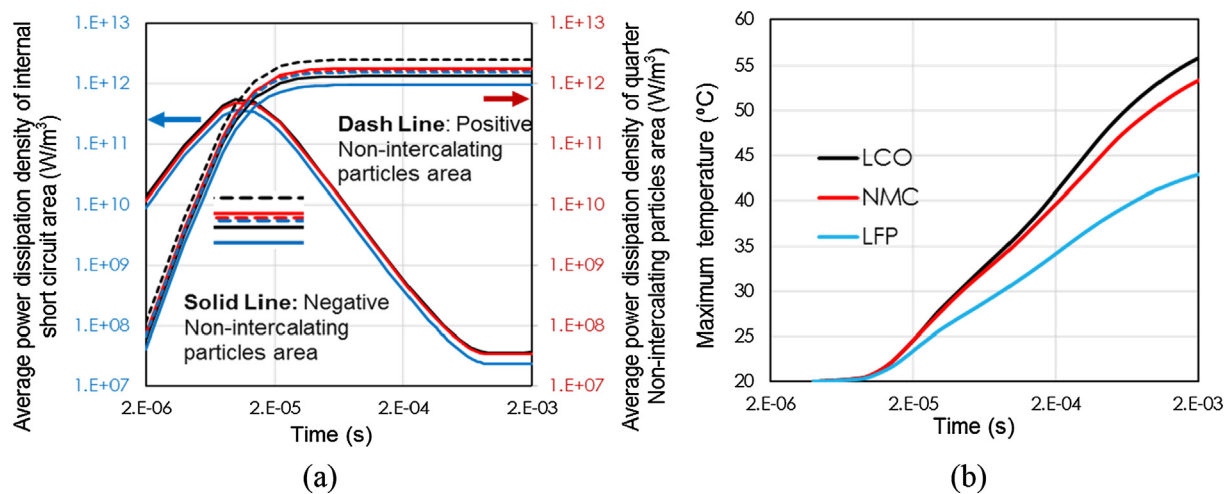


Fig. 7. Identification heat release and thermal response during a typical ISC event: (a) average heat release rate evolution in the ISC and the non-intercalating particle areas (b) Maximum temperature rise of different battery materials during the current ISC event.

release rate and higher heat capacity.

3.5. Combined analysis of ISC and thermal runaway

In the real situation, electrochemical reactions quickly heat up the battery structure which further triggers the thermal runaway chemistry. Such simulation is achieved in a decouple-recombine manner in the current work. With the heat release rate separately evaluated from the electrochemistry, it becomes feasible to combine the results from the ISC modeling and the thermal runaway modeling, and to eventually answer the question if the ISC event is able to trigger thermal runaway or not. Specifically, the peak heat release rate history shown in Fig. 7(a) could be assigned as the intensity of the hot spot in thermal runaway modeling. As shown in Fig. 8, runaway occurs right before 1 ms as shown by the instantaneous sharp temperature rise, which is very close to the relaxation time of the electrical field equilibrium in Fig. 7(a). Such consistency not only shows that thermal runaway will occur in this typical ISC scenario, but also adds to great confidence in the usage of both models, given that they are separately developed and validated against different types of measurement.

Recent findings have shown that internal short circuits are responsible for very little ($\sim 10\%$) of the total heat generated during thermal runaway, although they contribute to triggering the redox reactions after the separator collapses [14,15]. Without comparing the

ISC heat release and the total heat release during thermal runaway, our work focuses on the evaluation of the local heat release rate from the electrochemical reactions during ISC, and its relevance to the critical heat source intensity needed to trigger thermal runaway. Obviously, the total heat release during the entire process of thermal runaway is a much larger value and substantially depends on the enthalpy of formation of battery materials. It is noted that while complex interaction between electrochemistry and thermal runaway can exist in a typical event of ISC induced thermal runaway, our results help to bridge the two and to develop physics-based models for this important phenomena.

4. Conclusions

This work is a comprehensive computational study to identify the safety regime of Li-ion batteries. The concept of critical thermal runaway state is demonstrated, which is characterized by the critical heat source intensity and duration time. Below the critical state, thermal runaway cannot occur either due to insufficient heat source intensity or residence time. By exploring different critical states and connecting them, a safety regime diagram is identified and extended to further incorporate the effect of heat source size and material dependence.

The chemical kinetic feature during thermal runaway is identified through detailed comparison of runaway and non-runaway cases. It is found that the negative electrode – electrolyte reaction has a unique heat release profile, and directly correlate to thermal runaway. Normalized sensitivity analysis has been conducted to evaluate the key thermal-physical-chemical parameters for thermal runaway delay time, and the results show the delay time is more sensitive to the positive electrode-electrolyte reaction, in terms of its activation energy and frequency factor. The results here provide useful insights into the key factors, as well as direct guidance on how to validate the thermal runaway models.

To evaluate the potential of thermal runaway induced by ISC, a comprehensive thermal-electrochemical model is used to simulate the heat release rate from a typical ISC event. It is seen that in the initial period, the maximum heat release rate occurs in the metal region; as the electrical field approaches equilibrium, dominant heat release comes from the non-intercalating particle region, which could be as high as $1.E+12 \text{ W/m}^3$. This heat release rate profile is assigned as the intensity of the hot spot in thermal runaway modeling, which shows that thermal runaway is successfully triggered. The consistency in thermal runaway time and the electrical relaxation time suggests the consistency and validity of both models. Our results help to bridge the electrochemistry and thermal runaway in the event of ISC induced thermal runaway and

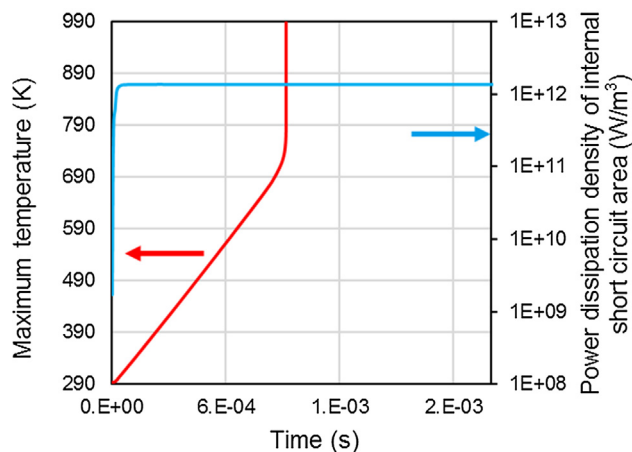


Fig. 8. Evolution of local maximum heat release rate during ISC, and the battery temperature evolution using the thermal runaway model, demonstrating the combined effect of the ISC model and the thermal runaway model.

to develop physics-based models for this important yet complex phenomena.

CRediT authorship contribution statement

Liwen Zhang: Methodology, Software, Validation, Investigation, Data curation, Visualization. **Peng Zhao:** Conceptualization, Methodology, Formal analysis, Visualization, Resources, Writing - original draft, Writing - review & editing, Supervision, Project administration. **Meng Xu:** Methodology, Software. **Xia Wang:** Methodology, Resources, Writing - review & editing.

Declaration of Competing Interest

The authors declare that they have no known competing financial interests or personal relationships that could have appeared to influence the work reported in this paper.

Acknowledgement

The authors appreciate the invited opportunity to present earlier versions of this research at the 9th Battery Safety Annual and 2019 COMSOL Day at Southfield, MI. PZ appreciates the partial support from the Rosen Dissertation Supervision Fellowship for this research.

Declaration of Competing Interest

None.

Appendix A. Supplementary material

Supplementary data to this article can be found online at <https://doi.org/10.1016/j.apenergy.2019.114440>.

References

- [1] Annual Energy Outlook 2019 with projections to 2050, US Energy Information Administration, www.eia.gov/ao, accessed on May 31, 2019.
- [2] Thackeray MM, Wolverton C, Isaacs ED. Electrical energy storage for transportation – approaching the limits of and going beyond, lithium-ion batteries. *Energy Environ Sci* 2012;5:7854–63.
- [3] Blomgren GF. The development and future of Lithium ion batteries. *J Electrochem Soc* 2017;164:A5019–25.
- [4] Placke T, Kloepsch R, Duhnen S, Winter M. Lithium ion, lithium metal, and alternative rechargeable battery technologies: the odyssey for high energy density. *J Solid State Electrochem* 2017;21:1939–64.
- [5] Broussely M, Biensan Ph, Bonhomme F, Blanchard Ph, Herreyre S, Nechev K, et al. *J Power Sources* 2005;146:90–6.
- [6] Zhao K, Pharr M, Vlassak JJ, Suo Z. Fracture of electrodes in lithium-ion batteries caused by fast charging. *J Appl Phys* 2010;108:073517.
- [7] Love CT, Baturina OA, Swider-Lyons KE. Observation of lithium dendrites at ambient temperature and below. *ECS Electrochem Lett* 2015;4:A24–7.
- [8] Xu Z, Xu M, Wang X, Zhao P. Conductive heating of Li-ion batteries at low temperatures. *ASME International Mechanical Engineering Congress and Exposition*, 6B:V06BT08A020. doi: 10.1115/IMECE2018-88235.
- [9] Liu B, Jia Y, Li J, Yin S, Yuan C, Hu Z, et al. Safety issues caused by internal short circuits in lithium-ion batteries. *J Mater Chem A* 2018;6:21475–84.
- [10] Simeone A, Lv D, Liu X, Zhang J. Collision damage assessment in lithium-ion battery cells via sensor monitoring and ensemble learning. *Procedia CIRP* 2018;78:273–8.
- [11] Larsson F, Andersson P, Blomqvist P, Loren A, Mellander B. Characteristics of lithium-ion batteries during fire tests. *J Power Sources* 2014;271:414–20.
- [12] Yuan Q, Zhao F, Wang W, Zhao Y, Liang Z, Yan D. Overcharge failure investigation of lithium-ion batteries. *Electrochim Acta* 2015;178:682–8.
- [13] Ren D, Liu X, Feng X, Lu L, Ouyang M, Li J, et al. Model-based thermal runaway prediction of lithium-ion batteries from kinetics analysis of cell components. *Appl Energy* 2018;228:633–44.
- [14] Feng X, Zheng S, Ren D, He X, Wang L, Cui H, et al. Investigating the thermal runaway mechanisms of lithium-ion batteries based on thermal analysis database. *Appl Energy* 2019;246:53–64.
- [15] Feng X, He X, Ouyang M, Wang L, Lu L, Ren D, et al. A coupled electrochemical-thermal failure model for predicting the thermal runaway behavior of lithium-ion batteries. *J Electrochem Soc* 2018;165:A3748–65.
- [16] Hatchard TD, MacNeil DD, Basu A, Dahn JR. Thermal model of cylindrical and prismatic lithium-ion cells. *J Electrochem Soc* 2001;148:A755–61.
- [17] Spotnitz R, Franklin J. Abuse behavior of high-power, lithium-ion cells. *J Power Sources* 2003;113:81–100.
- [18] Kim GH, Pesaran A, Spotnitz R. A three-dimensional thermal abuse model for lithium-ion cells. *J Power Sources* 2007;170:476–89.
- [19] Li J, Sun D, Jin X, Shi W, Sun C. Lithium-ion battery overcharging thermal characteristics analysis and an impedance-based electro-thermal coupled model simulation. *Appl Energy* 2019;254:113574.
- [20] Feng X, Ouyang M, Liu X, Lu L, Xia Y, He X. Thermal runaway mechanism of lithium ion battery for electric vehicles: a review. *Energy Storage Mater* 2018;10:246–67.
- [21] Peng P, Jiang F. Thermal safety of lithium-ion batteries with various cathode materials: a numerical study. *Int J Heat Mass Transfer* 2016;103:1008–1016.
- [22] Xu J, Lan C, Qiao Y, Ma Y. Prevent thermal runaway of lithium-ion batteries with minichannel cooling. *Appl Therm Eng* 2017;110:883–90.
- [23] Lopez CF, Jeevarajan JA, Mukherjee PP. Characterization of lithium-ion battery thermal abuse behavior using experimental and computational analysis. *J Electrochem Soc* 2015;162:A2163–73.
- [24] Ren D, Feng X, Lu L, Ouyang M, Zheng S, Li J, et al. An electrochemical-thermal coupled overcharge-to-thermal-runaway model for lithium ion battery. *J Power Sources* 2017;364:328–40.
- [25] Feng X, He X, Ouyang M, Lu L, Wu P, Kulp C, et al. Thermal runaway propagation model for designing a safer battery pack with 25 Ah LiNiCoMnO₂ large format lithium ion battery. *Appl Energy* 2015;154:74–91.
- [26] Santhanagopalan S, Ramadass P, Zhang J. Analysis of internal short-circuit in a lithium ion cell. *J Power Sources* 2009;194:550–7.
- [27] Chiu K, Lin C, Yeh S, Lin Y, Chen K. An electrochemical modeling of lithium-ion battery nail penetration. *J Power Sources* 2014;251:254–63.
- [28] Peng P, Sun Y, Jiang F. Thermal analyses of LiCoO₂ lithium-ion battery during oven tests. *Heat Mass Transf* 2014;50:1405–16.
- [29] Liang G, Zhang Y, Han Q, Liu Z, Jiang Z, Tian S. A novel 3D-layered electrochemical-thermal coupled model strategy for the nail-penetration process simulation. *J Power Sour* 2017;342:836–45.
- [30] Abada S, Petit M, Lecocq A, Marlaire G, Sauvart-Moynot V, Huet F. Combined experimental and modeling approaches of the thermal runaway of fresh and aged lithium-ion batteries. *J Power Sources* 2018;399:264–73.
- [31] Smith K, Wang CY. Power and thermal characterization of a lithium-ion battery pack for hybrid-electric vehicles. *J Power Sources* 2006;160:662–73.
- [32] Ye Y, Shi Y, Cai N, Lee J, He X. Electro-thermal modeling and experimental validation for lithium ion battery. *J Power Sources* 2012;199:227–38.
- [33] Wu B, Yufit Y, Marinescu M, Offer GJ, Martinez-Botas RF, Brandon NP. Coupled thermal-electrochemical modelling of uneven heat generation in lithium-ion battery packs. *J Power Sources* 2013;243:544–54.
- [34] Fang W, Ramadass P, Zhang ZJ. Study of internal short in a Li-ion cell-II. Numerical investigation using a 3D electrochemical-thermal model. *J Power Sources* 2014;248:1090–8.
- [35] Zavalis TG, Behm M, Lindbergh G. Investigation of short-circuit scenarios in a lithium-ion battery cell. *J Electrochem Soc* 2012;159:A848–59.
- [36] Xu M, Wang R, Reichman B, Wang X. Modeling the effect of two-stage fast charging protocol on thermal behavior and charging energy efficiency of lithium-ion batteries. *J Storage Mater* 2018;20:298–309.
- [37] Qu ZG, Li WQ, Tao WQ. Numerical model of the passive thermal management system for high-power lithium ion battery by using porous metal foam saturated with phase change material. *Int J Hydrogen Energy* 2014;39:3904–13.
- [38] Xu M, Zhang Z, Wang X, Jia L, Yang L. Two-dimensional electrochemical-thermal coupled modeling of cylindrical LiFePO₄ batteries. *J Power Sources* 2014;256:233–43.
- [39] Li X, Choe SY, Joe WT. A reduced order electrochemical and thermal model for a pouch type lithium ion polymer battery with LiNiMnCoO₂ – x – yO₂/LiFePO₄ blended cathode. *J Power Sources* 2015;294:545–55.
- [40] Rahn CD, Wang CY. Battery systems engineering. John Wiley & Sons; 2013.
- [41] Doyle M, Newman J, Gozdz AS, Schmutz CN, Tarascon JM. Comparison of modeling predictions with experimental data from plastic lithium ion cells. *J Electrochem Soc* 1996;143:1890–903.
- [42] Mei W, Chen H, Sun J, Wang Q. Numerical study on tab dimension optimization of lithium-ion battery from the thermal safety perspective. *Appl Therm Eng* 2018;142:148–65.
- [43] Li J, Cheng Y, Ai L, Jia M, Du S, Yin B, et al. 3D simulation on the internal distributed properties of lithium-ion battery with planar tabbed configuration. *J Power Sources* 2015;293:993–1005.
- [44] Gu WB, Wang CY. Thermal and electrochemical coupled modeling of a lithium-ion cell. *Proc ECS* 2000;99:748–62.
- [45] Mei W, Chen H, Sun J, Wang Q. The effect of electrode design parameters on battery performance and optimization of electrode thickness based on the electrochemical-thermal coupling model. *Sustain Energy Fuels* 2019;3:148–65.
- [46] Guo M, Sikha G, White RE. Single-particle model for a lithium-ion cell: Thermal behavior. *J Electrochem Soc* 2011;158:A122–32.
- [47] Zhao P, Lam S. Toward computational singular perturbation (CSP) without eigen-decomposition. *Combust Flame* 2019;209:63–73.
- [48] Jeon DH, Baek SM. Thermal modeling of cylindrical lithium ion battery during discharge cycle. *Energy Convers Manage* 2011;52:2973–81.
- [49] Xu M, Zhang Z, Wang X, Jia L, Yang L. A pseudo three-dimensional electrochemical-thermal model of a prismatic LiFePO₄ battery during discharge process. *Energy* 2015;80:303–17.
- [50] Chen Z, Burke M, Ju Y. On the critical flame radius and minimum ignition energy for spherical flame initiation. *Proc Combust Inst* 2011;33:1219–26.
- [51] Zhao P. Detailed kinetics in combustion simulation: manifestation, model reduction, and computational diagnostics. Springer; 2018. p. 45–71.
- [52] Vetter J, Petr Novak M, Wagner C, Veit K, Moller J, Besenhard M, et al. Ageing

- mechanisms in lithium-ion batteries. *J Power Sources* 2005;147:269–81.
- [53] Wang A, Kadam S, Li H, Shi S, Qi Y. Review on modeling of the anode solid electrolyte interphase (SEI) for lithium-ion batteries, *npj Comput. Mater* 2018;4:15.
- [54] Chen SC, Wan CC, Wang YY. Thermal analysis of lithium-ion batteries. *J Power Sources* 2005;140:111–24.
- [55] Feng X, Lu L, Ouyang M, Li J, He X. A 3D thermal runaway propagation model for a large format lithium ion battery module. *Energy* 2016;115:194–208.
- [56] Maleki H, Al S, Hallaj JR, Selman RB, Dinwiddie H Wang. Thermal properties of lithium-ion battery and components. *J Electrochem Soc* 1999;146:947–54.
- [57] Subramanian VR, Boovaragavan V, Ramadesigan V, Arabandi M. Mathematical model reformulation for lithium-ion battery simulations: Galvanostatic boundary conditions. *J Electrochem Soc* 2009;156:A260–71.
- [58] Jeon DH. Numerical modeling of lithium ion battery for predicting thermal behavior in a cylindrical cell. *Curr Appl Phys* 2014;14:196–205.
- [59] Kumaresan K, Sikha G, White RE. Thermal model for a Li-ion cell. *J Electrochem Soc* 2008;155:A164–71.
- [60] Fang W, Kwon OJ, Wang CY. Electrochemical–thermal modeling of automotive Li-ion batteries and experimental validation using a three-electrode cell. *Int J Energy Res* 2010;34:107–15.